ORIGINAL RESEARCH **Open access**

Model-Based Compensated Control of PMSM Drives with Stability Guarantees under Dynamic Variations

Gabriel Costa[1*], Rafael Mendes[1], Bruno Teixeira[2], Lucas Ribeiro[1]

Abstract

This study proposes a resilient control methodology utilizing a novel dynamic model that integrates the specifications of both the motor and the drive. The primary objective is to guarantee the steady operation of Permanent Magnet Synchronous Motor (PMSM) drives under parameter and DC link voltage fluctuations. Within this new control framework, the d-axis stator current error forms the initial segment of the drive's control law. The subsequent segment is formulated using the error derived from the squared q-axis stator current. To mitigate the negative impacts of fluctuations in rotor angular frequency and the discrepancy between load and electrical torque errors, specific compensators are implemented to handle the system's dynamic shifts. Additionally, the q-component of the control law incorporates a compensator dedicated to addressing errors in the drive's output power. Furthermore, a general operation curve (GOC) regarding the stator current is presented to offer deeper insights into the PMSM's performance. Subsequently, the study executes a thorough stability assessment, utilizing two closed-loop representations of the control scheme to confirm the stable functionality of both the q- and d-axis stator currents. To demonstrate the framework's effectiveness across multiple dynamic conditions, diverse MATLAB/SIMULINK simulations are supplied. Notably, comparative evaluations reveal that the introduced strategy outperforms traditional PI controllers. Specifically, it allows the PMSM torque and speed to achieve 50% and 95% of their target values in 42.9% and 28.6% less time, respectively. Furthermore, the proposed method yields a 75% reduction in torque and speed undershoot when contrasted with the standard PI regulator.

Keywords Permanent Magnet Synchronous Motor (PMSM), Stator currents, Compensators, General Operation Curve (GOC), Drive, DC link voltage and parameter variations

*Correspondence:
Gabriel Costa
gabriel.costa@ufrj.br
[1] Department of AI-Based Energy Systems, Faculty of Engineering, Federal University of Rio de Janeiro, Rio de Janeiro, Brazil
[2] Department of Smart Grid Engineering, Faculty of Engineering, University of Campinas, Campinas, Brazil

Introduction

Due to their highly efficient operation, compact design, reduced acoustic noise, elevated power density, and superior torque-to-current ratios, Permanent-Magnet Synchronous Motor (PMSM) drives have seen widespread adoption across numerous industrial sectors, including electric vehicles, ship propulsion, robotics, traction, aerospace, and renewable energy systems [1]. Recent literature has focused heavily on the control and dynamic modeling of PMSM drives powered by DC/AC voltage-source PWM converters to enable advanced performance improvements [2-8]. Examples of novel dynamical frameworks for PMSMs include a two-dimensional analytical thermal representation [5], a harmonic coupling configuration utilizing magnetic co-energy [6], a unified graphical approach [7], and a model reliant on iterative flux sliding-mode observation [8].

This is an open access article distributed under the terms of the Creative Commons Attribution-NonCommercial-ShareAlike 4.0 International License (CC BY-NC-SA 4.0), which permits non-commercial use, distribution, reproduction, and adaptation in any medium or format, provided that appropriate credit is given to the original author(s) and source, a link to the license is provided, and any changes made are indicated. Adapted material must be distributed under the same license.

© 2024 The Author(s). | Published by Institute of Smart Energy Systems Press

Continuing this line of inquiry, several other studies have also explored PMSM dynamic modeling. Inoue *et al*. [9] introduced a mathematical framework for the PMSM drive that accounted for cross-magnetization and magnetic saturation effects. This representation facilitated the creation of a maximum torque per ampere (MTPA) control mechanism within the synchronous frame of the stator flux linkage [9]. The geometric structural uncertainties of the PMSM were linearized in Cai *et al.* [10] to derive a novel mathematical model, which was subsequently utilized to formulate a linear time-invariant (LTI) two-input-two-output (TITO) control system. To detect rotor motion over a specified control timeframe, a straightforward mathematical model—incorporating linear current variations under steady supply voltages—was applied to a high-speed PMSM drive in Jarzebowicz [11]. The aforementioned representations, however, neglected the nonlinear characteristics of the PMSM drive, as well as the combined dynamic equations of the motor and the drive itself. The present manuscript aims to address these limitations. Beyond formulating a suitable dynamic model, developing an efficient control architecture remains a critical hurdle in achieving precise PMSM performance. A control methodology rooted in maximum torque per peak current and dual three-phase PMSM torque modeling was established in Feng *et al*. [12]. Furthermore, to precisely regulate the PMSM and estimate combined disturbances, Liu and Li [13] crafted an optimal, simplified model-based control law that merged the predictive functional control (PFC) with the extended state observer (ESO) technique.

Control schemes exhibiting robust characteristics are inherently prioritized across diverse PMSM operational states. Real-time adjustment of model parameter mismatches via weight coefficients was achieved through a new current predictive controller utilizing a fuzzy algorithm in Wang *et al*. [14]. Similarly, sliding-mode control paradigms have been engineered specifically to target PMSM parameter inconsistencies [15-19]. To minimize torque fluctuations, Liu *et al.* [20] developed a sliding-mode-based iterative learning controller functioning alongside a standard proportional-integral (PI) regulator. Robust reference-tracking capability was secured for the PMSM drive by merging disturbance cross-coupling compensation into a discrete-time sliding-mode current controller [21]. This approach also incorporated a discrete-time backstepping disturbance observer to bolster tracking and resilience [21]. Considering time-domain responses and THD for pump applications, Ganapathee *et al.* [22] used an optimal hybrid controller and space vector modulation to govern a DC-powered inverter, thereby regulating the PMSM's current and speed. By integrating voltage commands with a straightforward feedforward component, Xu *et al.* [23] proposed a robust controller. This solution reduced sensitivity to high-frequency noise while improving stability against parameter mismatches.

To curtail PMSM torque oscillations amid parameter shifts, an optimal stator current formulation was devised in Lai *et al.* [24]. Distinct from standard parameter discrepancies [25], fluctuations in the DC link voltage necessitate the inclusion of an additional robustness module within the PMSM control architecture. Such a module is highly applicable to satellite reaction wheels [26], electric/hybrid vehicles [27], constant power loads [28], and flywheel energy storage systems [29]. A filterless offset suppression technique was proposed in Yuan and Zhao [30] to successfully manage adjustable-speed PMSM drives experiencing DC-link capacitor voltage offsets. To govern a quasi-Z-Source inverter-driven PMSM subjected to the combined impacts of power variations and DC-link voltage shifts, Shuai *et al*. [31] suggested a composite control method. Ke *et al*. [32] introduced a strategy pairing a voltage regulator with a modulation index controller to stabilize the PMSM DC voltage. This approach rapidly discharges the DC bus while preventing its recharge regardless of the machine's speed. A wide array of alternative robust and nonlinear control strategies featuring diverse observers have been tailored for PMSMs across various operational states. Notable examples include adaptive backstepping sliding-mode controllers paired with nonlinear observers [33], two-degree-of-freedom PI regulators utilizing disturbance observers [34], fractional-order PID systems incorporating Bode's ideal cutoff filter [35], adaptive optimal configurations offering uncertainty and disturbance attenuation [36], model predictive current control partnered with model-aided extended state observers [37], and double control strategies utilizing resolvers [38]. Furthermore, alternative control methodologies have been extended to other motor categories, encompassing adaptive fractional-order PID frameworks driven by the Artificial Bee Colony algorithm for brushless DC motors [39], fractional-order PIλ controllers utilizing the Whale Optimization algorithm for brushless DC motors [40], and nonlinear optimal multi-loop flatness-based strategies for induction motors [41].

© 2024 The Author(s). | Published by Institute of Smart Energy Systems Press

Prior research has failed to account for the concurrent fluctuation of the DC-link voltage, PMSM drive parameters, and drive parameter mismatches. This article introduces a control scheme designed to rectify these oversights by properly tuning the operational conditions of a PMSM drive when confronted with simultaneous changes in both parameters and DC-link voltage. The primary contributions of this work are highlighted below:

(1) Introducing a novel dynamic framework that fuses the dynamic attributes of both the drive and the PMSM, substituting the rotor angular frequency with its dynamic behavior alongside the load and electrical torques.

(2) Formulating a controller grounded in the compensation of errors found in the d-component and the squared q-component of the PMSM stator currents.

(3) Bolstering the dynamic responsiveness of the devised controller by minimizing the adverse influences of variations in rotor angular frequency and the gap between load and electrical torque errors.

(4) Adjusting for errors in the drive's output power via the q-axis of the suggested control framework.

(5) Guaranteeing the stable functionality of the PMSM drive amidst the simultaneous shifting of the DC-link voltage and drive parameters.

(6) Establishing, for the first time, a General Operation Curve (GOC) for drive-integrated PMSMs utilizing the motor's stator currents.

Proposed Control Technique for PMSM Drive

Figure 1 illustrates the overarching architecture of the drive-integrated PMSM examined throughout this study. Operating as the system's input, the DC link voltage must be maintained at a steady magnitude. The dynamic equations governing the PMSM, taking into account the rotor angular frequency and stator windings, are expressed as [42],

$$L_s \frac{di_d}{dt} + R_s i_d - L_s p \omega_r i_q = v_d \quad (1)$$

$$L_s \frac{di_q}{dt} + R_s i_q + L_s p \omega_r i_d + \varphi p \omega_r = v_q \quad (2)$$

$$J \frac{d\omega_r}{dt} + \beta \omega_r = T_e - T_L \quad (3)$$

$$T_e = 1.5 p \varphi i_q \quad (4)$$

Similarly, the dynamic formulas for the three-phase DC/AC converter functioning as the drive for the PMSM are detailed as [43],

$$L_c \frac{di_d}{dt} + R_c i_d - \omega L_c i_q - u_d v_{dc} + v_d = 0 \quad (5)$$

$$L_c \frac{di_q}{dt} + R_c i_q + \omega L_c i_d - u_q v_{dc} + v_q = 0 \quad (6)$$

© 2024 The Author(s). | Published by Institute of Smart Energy Systems Press

$$C\frac{dv_{dc}}{dt} + u_d i_d + u_q i_q - i_{dc} = 0 \quad (7)$$

It is known that $\omega = p\omega r$. Through the merging of (1), (5) along with (2), (6), a consolidated set of equations incorporating the traits of both the drive and the PMSM is formulated as,

$$(L_c - L_s)\frac{di_d}{dt} + (R_c - R_s)i_d - (L_c - L_s)p\omega_r i_q - u_d v_{dc} + 2v_d = 0 \quad (8)$$

$$(L_c - L_s)\frac{di_q}{dt} + (R_c - R_s)i_q + (L_c - L_s)p\omega_r i_d - \varphi p\omega_r - u_q v_{dc} + 2v_q = 0 \quad (9)$$

Conversely, deriving from **Eqs. 3 and 4**, the rotor angular frequency and flux are acquired as follows,

$$\varphi = \frac{T_e}{1.5pi_q} \quad (10)$$

$$\omega_r = \frac{1}{\beta}T_e - \frac{1}{\beta}T_L - \frac{J}{\beta}\frac{d\omega_r}{dt} \quad (11)$$

Inserting **Eqs. 10 and 11** into **Eqs. 8 and 9** yields the subsequent dynamic relationships for the drive-integrated PMSM,

$$(L_c - L_s)\frac{di_d}{dt} + (R_c - R_s)i_d - (L_c - L_s)pi_q\left(\frac{1}{\beta}T_e - \frac{1}{\beta}T_L - \frac{J}{\beta}\frac{d\omega_r}{dt}\right) - u_d v_{dc} + 2v_d = 0 \quad (12)$$

$$\begin{aligned}&\tfrac{1.5}{2}p(L_c - L_s)\tfrac{di_q^2}{dt} + 1.5p(R_c - R_s)i_q^2 - 1.5pi_q u_q v_{dc}\\ &-T_e p\omega_r + 1.5p^2(L_c - L_s)\left(\tfrac{1}{\beta}T_e - \tfrac{1}{\beta}T_L - \tfrac{J}{\beta}\tfrac{d\omega_r}{dt}\right)i_d i_q + 3pi_q v_q = 0\end{aligned} \quad (13)$$

Applying **Eqs. 5 and 6** alongside **Eqs. 12 and 13** establishes two closed-loop configurations, which graphically represent the d and q segments of the formulated control strategy for the PMSM drive, as portrayed in **Figures 2a and 2b**, respectively.

As indicated by **Figure 2a**, the control law's d-axis component is managed via two PI and Gcd (s) compensators, which are deployed to rectify the d-axis stator current error and the rotor angular frequency, respectively. Furthermore, this specific control element regulates the variance between load and electrical torque errors utilizing the coefficient $k\beta d$. Conversely, as shown in **Figure 2b**, formulating the q-axis control component involves tuning a PI controller, $Gcq1$ compensator, and $k\beta$q to reduce the squared q-axis stator current error systematically, the rotor angular frequency error, and the discrepancy between load and electrical torque errors, respectively. Compared with the d-axis framework, an extra compensator is integrated into the q-axis design to manage discrepancies in the drive's output power, as shown in **Figure 2b.**

© 2024 The Author(s). | Published by Institute of Smart Energy Systems Press

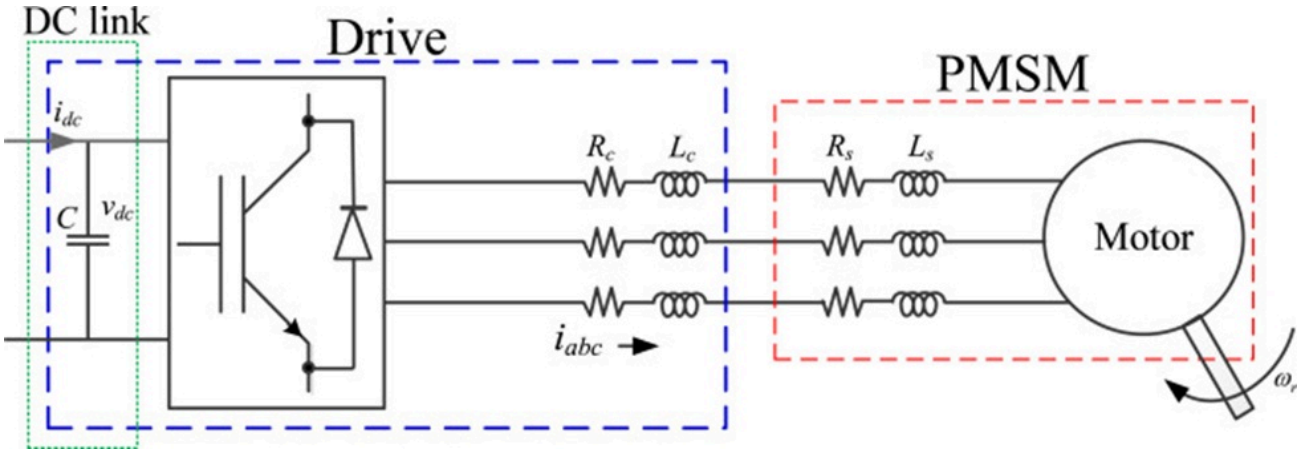
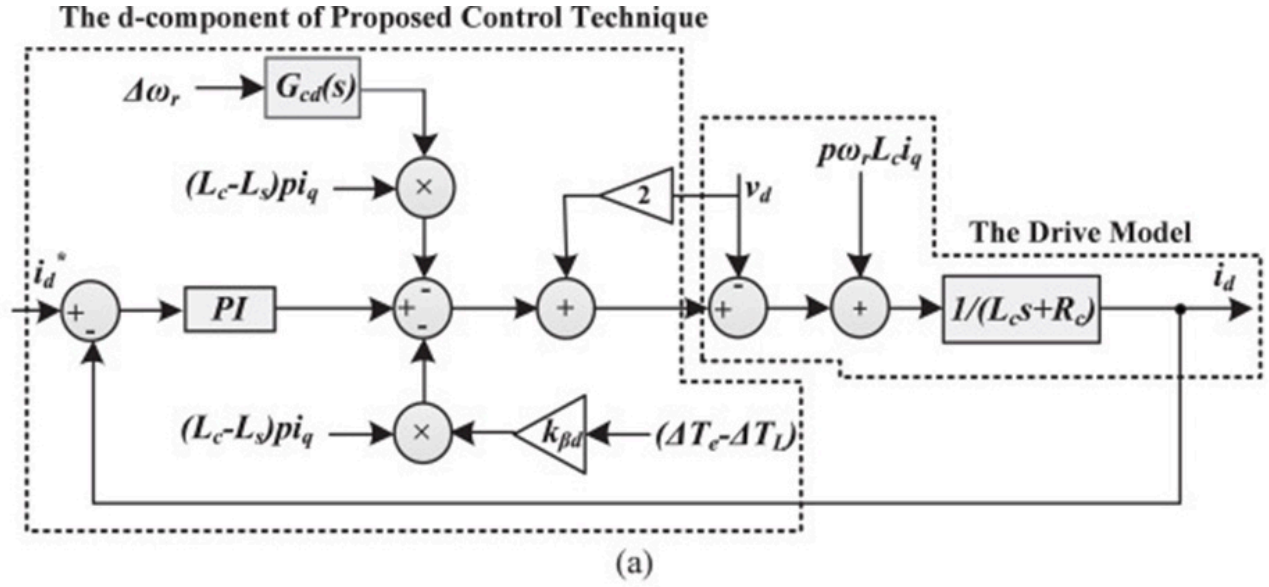
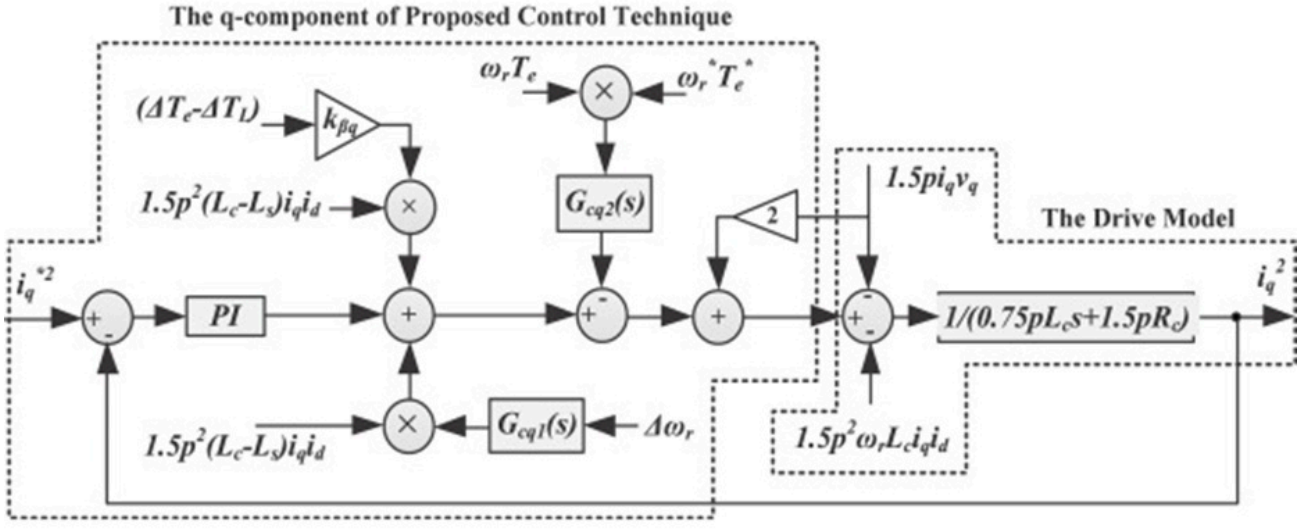


Figure 1. General structure of PMSM drive under study.



(a)



(b)

© 2024 The Author(s). | Published by Institute of Smart Energy Systems Press

Figure 2. The closed-loop systems of the proposed control technique for PMSM drive, (a) d-component, and (b) q-component.

The Proposed General Operation Curve (GOC) for PMSM Stator Currents

This section introduces a generalized operating curve (GOC) designed to define the functional boundaries of the PMSM stator currents within the d-q rotating frame. To establish this boundary, the respective control expressions for the d-axis and q-axis of the motor drive are derived from **Eqs. 8 and 9** in the following manner:

$$u_d = \left[\left(L_c - L_s\right)\tilde{i}_d + \left(R_c - R_s\right)i_d - \left(L_c - L_s\right)p\omega_r i_q + 2v_d\right]/v_{dc} \quad (14)$$

$$u_q = \begin{bmatrix} \left(L_c - L_s\right)\tilde{i}_q + \left(R_c - R_s\right)i_q + \left(L_c - L_s\right)p\omega_r i_d \\ -\varphi p\omega_r + 2v_q \end{bmatrix}/v_{dc} \quad (15)$$

By substituting expressions **Eqs. 14 and 15** directly into **Eq. 7**, the mathematical framework for the projected GOC governing the stator currents in the d-q plane is established as:

$$\left(i_q - c_d\right)^2 + \left(i_d - c_q\right)^2 = r^2 \quad (16)$$

In this formulation, the coordinate pair C = (cd, cq) defines the geometric center, whereas r denotes the corresponding radius of the GOC profile. These structural parameters satisfy the relations below:

$$\begin{aligned} c_d &= -\left(\frac{v_d}{\left(R_c - R_s\right)} + \frac{\left(L_c - L_s\right)\tilde{i}_d}{2\left(R_c - R_s\right)}\right) \\ c_q &= -\left(\frac{\left(L_c - L_s\right)}{2\left(R_c - R_s\right)}\tilde{i}_q - \frac{\varphi p\omega_r}{2\left(R_c - R_s\right)} + \frac{v_q}{\left(R_c - R_s\right)}\right) \\ r &= \sqrt{\begin{aligned} &\frac{v_{dc}i_{dc}}{\left(R_c - R_s\right)} - \frac{Cv_{dc}\tilde{v}_{dc}}{\left(R_c - R_s\right)} + \left(\frac{v_d}{\left(R_c - R_s\right)} + \frac{\left(L_c - L_s\right)\tilde{i}_d}{2\left(R_c - R_s\right)}\right)^2 \\ &+ \left(\frac{\left(L_c - L_s\right)}{2\left(R_c - R_s\right)}\tilde{i}_q - \frac{\varphi p\omega_r}{2\left(R_c - R_s\right)} + \frac{v_q}{\left(R_c - R_s\right)}\right)^2 \end{aligned}} \end{aligned} \quad (17)$$

Eq. 17 demonstrates that the baseline attributes of the GOC depend heavily on a combination of machine and drive parameters, the instantaneous DC-bus voltage alongside its time derivative, the permanent magnet flux linkage, the rotor speed, and both the d- and q-axis voltage components. The behavior of this curve under fluctuating drive parameters is illustrated in **Figures 3a and 3b**. Examination of **Figure 3a** indicates that elevating the resistance Rc causes a prominent contraction of the permissible operating zone for the PMSM. Conversely, an upward shift in the inductance Lc exerts minimal influence on the positional parameters of the GOC, as highlighted in **Figure 3b.**

Leveraging this geometric concept, **Figure 4** charts the boundary limits of the DC-link voltage and its derivative under the constraint where the d-axis current deviations contract toward zero. In this state, the DC-bus voltage is restricted to a narrower operational envelope. Consequently, the PMSM performance profile remains highly stable, with virtually no fluctuations, as shown in **Figure 4a.** This implies that as the motor state trajectories converge toward their steady-state references, the DC-link voltage exhibits no significant deviation. A corresponding pattern is observed for the time derivative of the DC-link voltage, which successfully reduces to zero when the system reaches a stable equilibrium, as visualized in **Figure 4b.**

© 2024 The Author(s). | Published by Institute of Smart Energy Systems Press

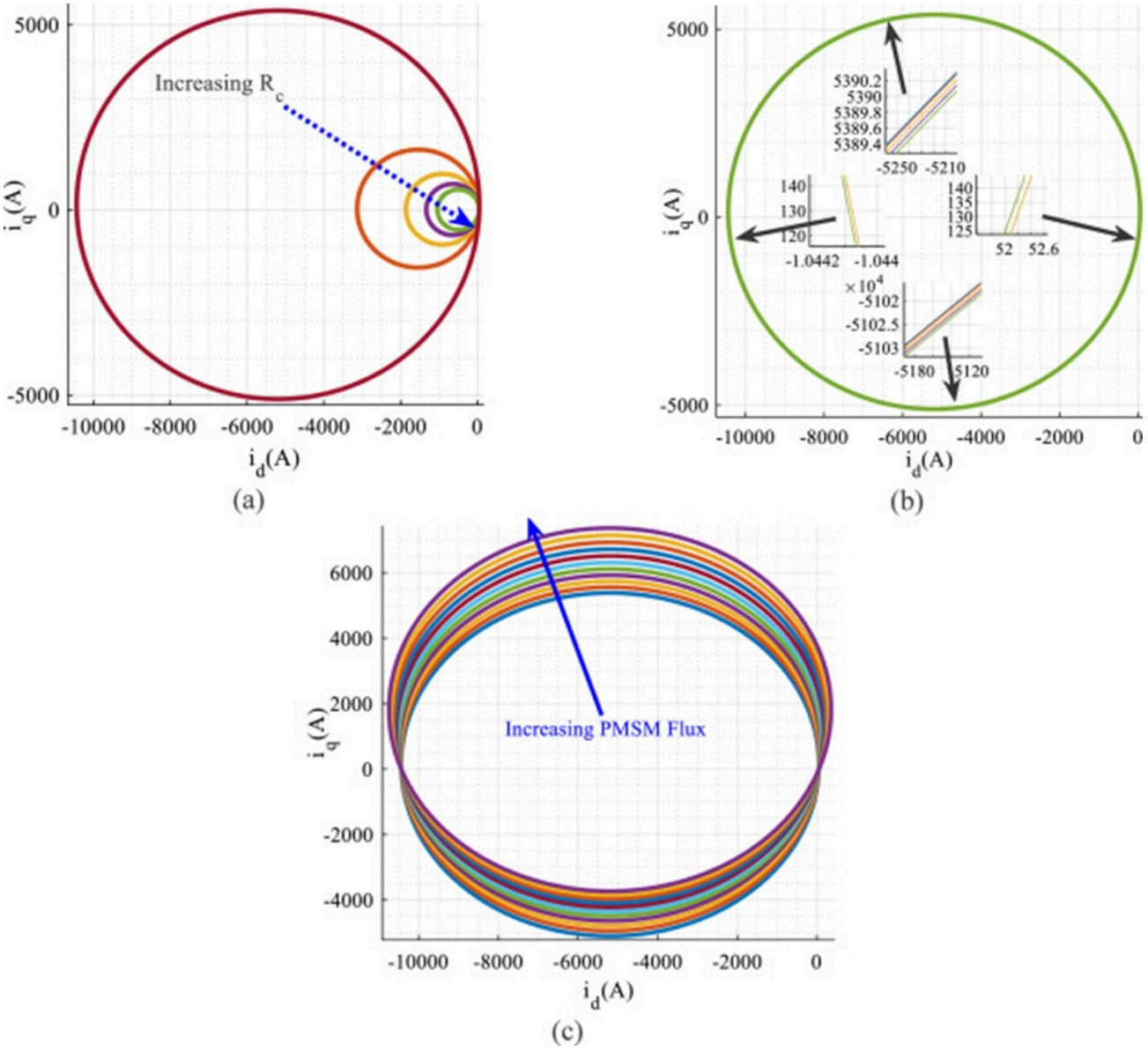


Figure 3. The proposed GOC under (a) the increment of Rc, (b) the increment of Lc, and (c) the increment of magnetic flux.

© 2024 The Author(s). | Published by Institute of Smart Energy Systems Press

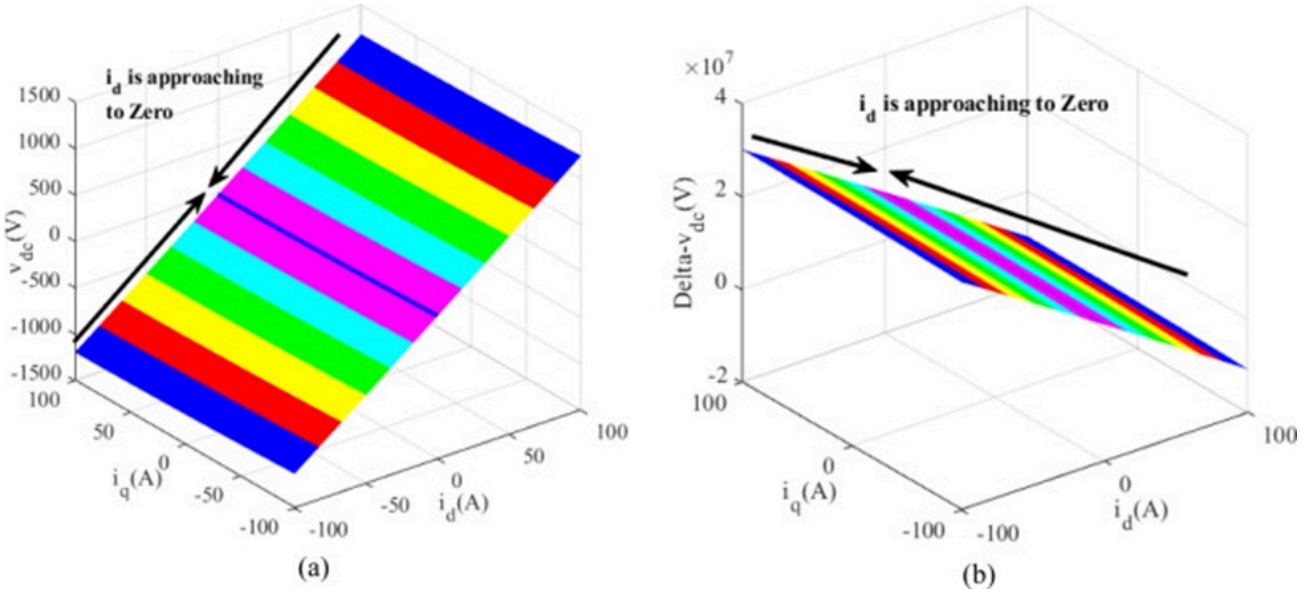


Figure 4. 3D-curves of PMSM stator currents in the dq reference frame under (a) DC link voltage variations, and (b) the variations of the derivative of DC-link voltage.

Stability Evaluation Under Inaccurate Parameters and PI-Regulator Effects

Proper tuning of the controller gains is essential to guarantee that the machine currents track their command values with minimal delay. Accordingly, gain selection is executed under the assumption of plant parameter mismatches. automotive-grade loop compensation is established by applying a Proportional-Integral (PI) regulator to every control block in **Figure 2**, governed by:

$$G_{cd}(s) = k_{pod} + k_{iod}/s \quad (18)$$

$$G_{cq1}(s) = k_{poq} + k_{ioq}/s, G_{cq2}(s) = k_{pq2} + k_{iq2}/s \quad (19)$$

Additionally, the current loop PI structures for the d- and q-axes are defined as k_{pd} + k_{id} /s and k_{pq} + k_{iq} /s, respectively. Based on these considerations, a comparative analysis is presented to justify the selection of standard PI structures over pure integral control configurations.

Rotor angular frequency variations

As illustrated in the block diagram of **Figure 2**, precise rejection of the speed error is required to optimize the d- and q-axis trajectories within the new control laws. By evaluating the closed-loop architectures in **Figures 2a and 2b**, the following pair of transfer functions can be established:

© 2024 The Author(s). | Published by Institute of Smart Energy Systems Press

$$\left[\frac{i_d}{\Delta\omega_r}\right]^2 = \left[p^2 i_q^{*2}\left(L_c' - L_s'\right)^2\right] \times \frac{\left[k_{pod}^2 k_{pq} s^3 + \left[\begin{array}{l} 2k_{pood}k_{iood}k_{pq} \\ +k_{pood}^2 k_{iq} \end{array}\right] s^2 + \left[\begin{array}{l} k_{iood}^2 k_{pq} + \\ 2k_{pood}k_{iood}k_{iq} \end{array}\right] s + k_{iood}^2 k_{iq}\right]}{\left[\begin{array}{l} 0.75L_c'^3 p s^6 + L_c'^2\left[1.5p\left(R_c' + k_{pd}\right) + \left(1.5pR_c' + k_{pq}\right)\right] s^5 \\ + \left[0.75pL_c'\left[\left(R_c' + k_{pd}\right)^2 + 2L_c' k_{id}\right] + 2L_c'\left(R_c' + k_{pd}\right)\left(1.5pR_c' + k_{pq}\right) + L_c'^2 k_{iq}\right] s^4 \\ + \left[1.5k_{id}pL_c'\left(R_c' + k_{pd}\right) + 2L_c'\left(R_c' + k_{pd}\right)k_{iq} + \left[\left(R_c' + k_{pd}\right)^2 + 2L_c' k_{id}\right]\left(1.5pR_c' + k_{pq}\right)\right] s^3 \\ + \left[0.75pL_c' k_{id}^2 + \left[\left(R_c' + k_{pd}\right)^2 + 2L_c' k_{id}\right] k_{iq} + 2k_{id}\left(R_c' + k_{pd}\right)\left(1.5pR_c' + k_{pq}\right)\right] s^2 \\ + \left[k_{id}^2\left(1.5pR_c' + k_{pq}\right) + 2\left(R_c' + k_{pd}\right)k_{id}k_{iq}\right] s + k_{id}^2 k_{iq} \end{array}\right]} \quad (20)$$

$$\frac{i_q}{\Delta\omega_r} = 1.5p^2 i_d^*\left(L_c' - L_s'\right) \times \frac{\left[k_{pd}k_{pooq}s^2 + \left[k_{id}k_{pooq} + k_{iooq}k_{pd}\right]s + k_{iooq}k_{id}\right]}{\left[\begin{array}{l} 0.75pL_c'^2 s^4 + L_c'\left[\left(1.5pR_c' + k_{pq}\right) + 0.75p\left(R_c' + k_{pd}\right)\right] s^3 \\ + \left[k_{iq}L_c' + \left(1.5pR_c' + k_{pq}\right)\left(R_c' + k_{pd}\right) + 0.75pL_c' k_{id}\right] s^2 + \\ \left[k_{iq}\left(R_c' + k_{pd}\right) + \left(1.5pR_c' + k_{pq}\right)k_{id}\right] s + k_{iq}k_{id} \end{array}\right] \quad (21)$$

Where $L'_{c(s)} = {}_{(s)} + \Delta_{(s)}$ and $R'_{c(s)} = R_{c(s)} + \Delta R_{c(s)}$. The terms (s) and $\Delta(s)$ quantify the parameter deviations within the electrical drive and the motor. The corresponding Nyquist curves for **Eq. 20** are displayed in **Figures 4a and 4b.** As revealed by **Figure 4a**, under nominal conditions (zero parameter mismatch), the developed PI-based control architecture yields significantly lower id perturbations than a pure integral control approach. This confirms that the influence of speed fluctuations on the d-axis motor current becomes trivial when PI structures serve as the primary compensators in the architecture of **Figure 2.**

In the event of a 100% parametric shift (where $L'_{c(s)} = 2_{(s)}$ and $R'_{c(s)} = 2_{(s)}$), the proposed PI-driven methodology continues to maintain a lower d-axis current variance compared to pure integral mechanisms. Furthermore, the response characteristics shown in **Figure 4b** offer a path to further fortify the robustness of the PI-based design. Specifically, increasing the control-loop gains enables the current-loop id to enhance its relative stability threshold considerably. To provide deeper insight, **Figure 4c** presents the root locus trajectories for expression (21) under fluctuating plant and compensator profiles. This diagram illustrates that the new PI-based scheme provides a superior stability margin under both nominal (0%) and degraded (100%) parameter scenarios relative to an unperturbed system utilizing basic integral regulation. Accordingly, the evidence confirms that employing PI structures instead of simple integral blocks guarantees a more robust response and improved stability margins for the current id when dealing with uncertain plant dynamics **(Figure 5).**

© 2024 The Author(s). | Published by Institute of Smart Energy Systems Press

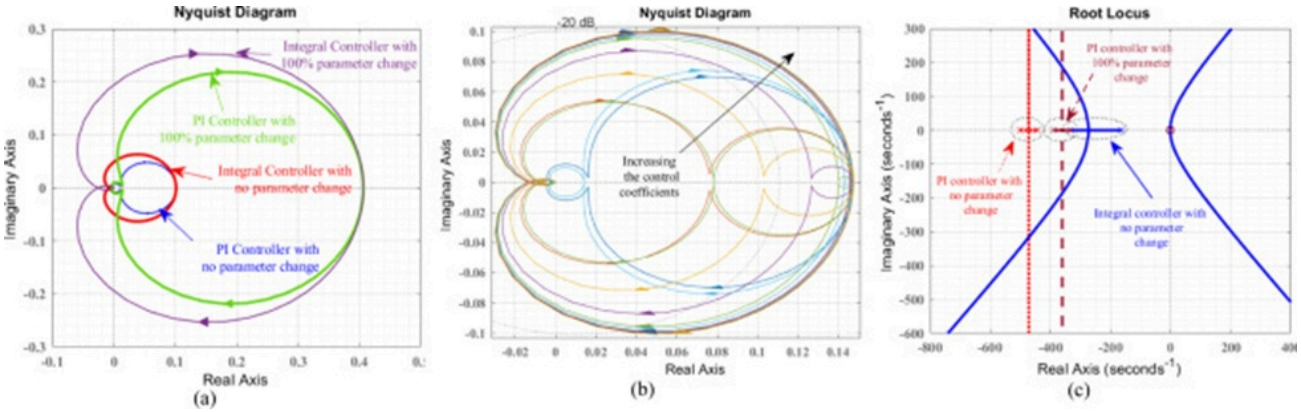


Figure 5. (a) The Nyquist diagrams of $(i_d/\Delta\omega_r)^2$ when PMSM parameters and compensators are changed, (b) The Nyquist diagrams of $(id/\Delta\omega r)2$ when the controller coefficients are increased, and (c) The root locus diagrams of $(i_q/\Delta\omega_r)$ when PMSM parameters and compensators are changed.

Difference between electrical and load torque errors

This subsection analyzes the response characteristics of the q-axis current loop. By examining the structural interactions in **Figures 2a and 2b**, the transfer functions relating to the current iq are formulated as follows:

$$\left(\frac{i_d}{\Delta T_e-\Delta T_L}\right)^2=\left[\left(L_c'-L_s'\right)^2p^2k_{\beta d}^2i_q^{*2}\right]\times \frac{\left[k_{pq}s^3+k_{iq}s^2\right]}{\begin{bmatrix}0.75L_c'^3ps^6+L_c'^2\left[1.5p\left(R_c'+k_{pd}\right)+\left(1.5pR_c'+k_{pq}\right)\right]s^5\\+\left[0.75pL_c'\left[\left(R_c'+k_{pd}\right)^2+2L_c'k_{id}\right]+2L_c'\left(R_c'+k_{pd}\right)\left(1.5pR_c'+k_{pq}\right)+L_c'^2k_{iq}\right]s^4\\+\left[1.5k_{id}pL_c'\left(R_c'+k_{pd}\right)+2L_c'\left(R_c'+k_{pd}\right)k_{iq}+\left[\left(R_c'+k_{pd}\right)^2+2L_c'k_{id}\right]\left(1.5pR_c'+k_{pq}\right)\right]s^3\\+\left[0.75pL_c'k_{id}^2+\left[\left(R_c'+k_{pd}\right)^2+2L_c'k_{id}\right]k_{iq}+2k_{id}\left(R_c'+k_{pd}\right)\left(1.5pR_c'+k_{pq}\right)\right]s^2\\+\left[k_{id}^2\left(1.5pR_c'+k_{pq}\right)+2\left(R_c'+k_{pd}\right)k_{id}k_{iq}\right]s+k_{id}^2k_{iq}\end{bmatrix}} \quad (22)$$

$$\frac{i_q}{\Delta T_e-\Delta T_L}=\frac{1.5p^2i_d^*\left(L_c'-L_s'\right)\times\left(k_{pd}k_{\beta q}s^2+k_{id}k_{\beta q}s\right)}{\begin{bmatrix}0.75pL_c'^2s^4+L_c'\left[\left(1.5pR_c'+k_{pq}\right)+0.75p\left(R_c'+k_{pd}\right)\right]s^3\\+\left[k_{iq}L_c'+\left(1.5pR_c'+k_{pq}\right)\left(R_c'+k_{pd}\right)+0.75pL_c'k_{id}\right]s^2+\\\left[k_{iq}\left(R_c'+k_{pd}\right)+\left(1.5pR_c'+k_{pq}\right)k_{id}\right]s+k_{iq}k_{id}\end{bmatrix}} \quad (23)$$

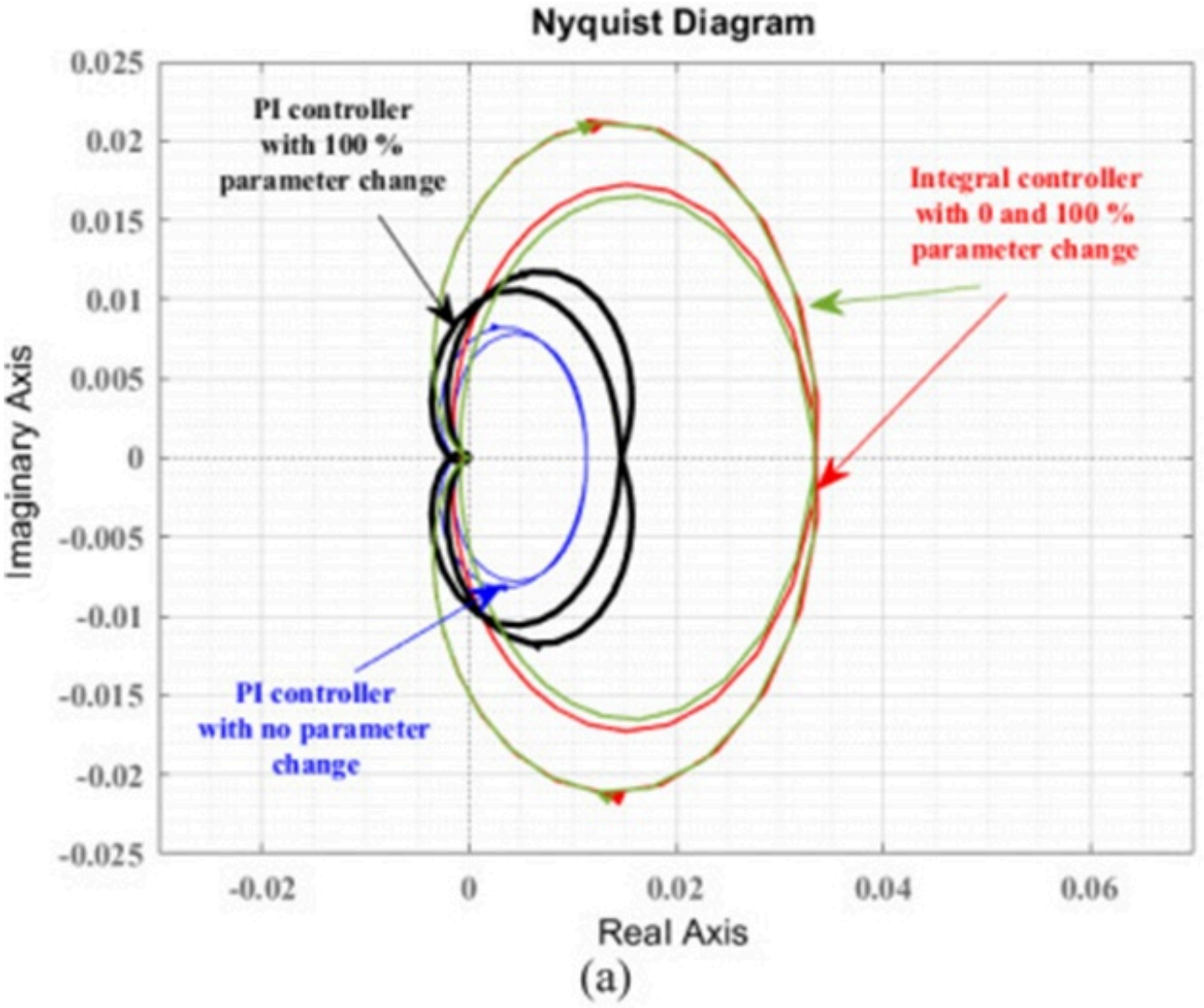
The Nyquist characteristics of expression (22) during modifications to the motor parameters and compensating loops are depicted in **Figure 6a.** As shown in this illustration, the developed resilient control framework exhibits substantially greater robustness than a design incorporating simple integral blocks in **Figure 2**. Remarkably, the performance of the PI-based strategy under a severe 100% parametric disturbance remains vastly superior to that of an integral configuration operating under completely nominal parameters. These findings demonstrate that utilizing PI blocks within the new control architecture effectively insulates the d-axis current from any variations in the net torque error, irrespective of plant parameter drift.

Additionally, when evaluating variations across the system variables, the performance of transfer **Eq. 23** mirrors the root-locus trends discussed for **Figure 5c.** Furthermore, **Figure 6b** indicates that optimal adjustment of the controller

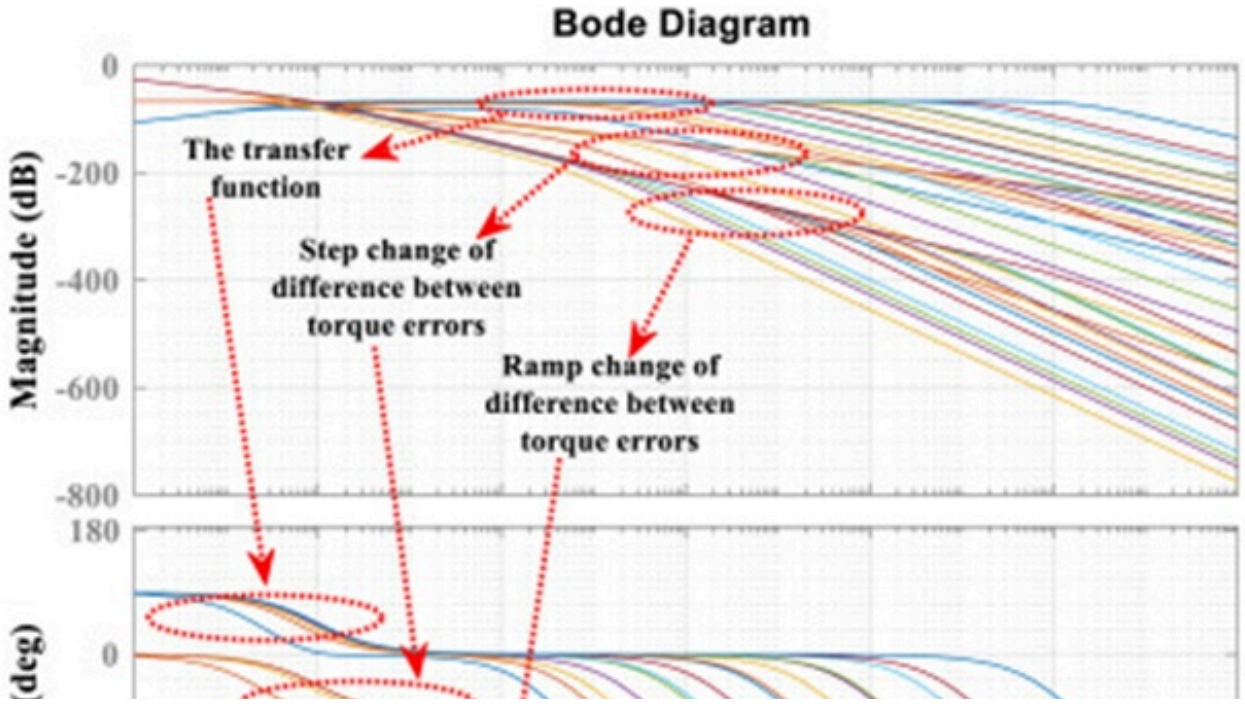
© 2024 The Author(s). | Published by Institute of Smart Energy Systems Press

parameters ensures the iq tracking error converges perfectly to zero when subjected to step or ramp disturbances in the net torque deviation. Compared to speed-induced perturbations, torque mismatches generate noticeably smaller transient deviations in the q-axis current trajectory, as detailed across **Figures.6a and 6b.**

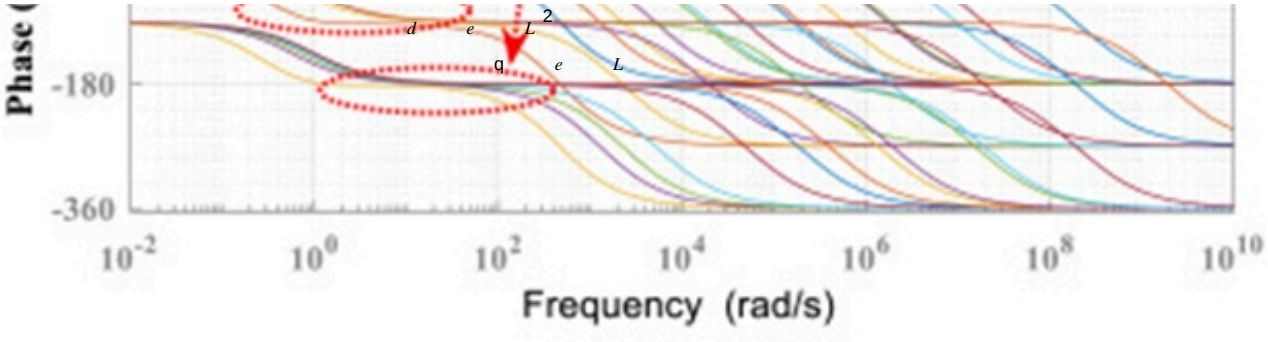
© 2024 The Author(s). | Published by Institute of Smart Energy Systems Press



(a)



© 2024 The Author(s). | Published by Institute of Smart Energy Systems Press



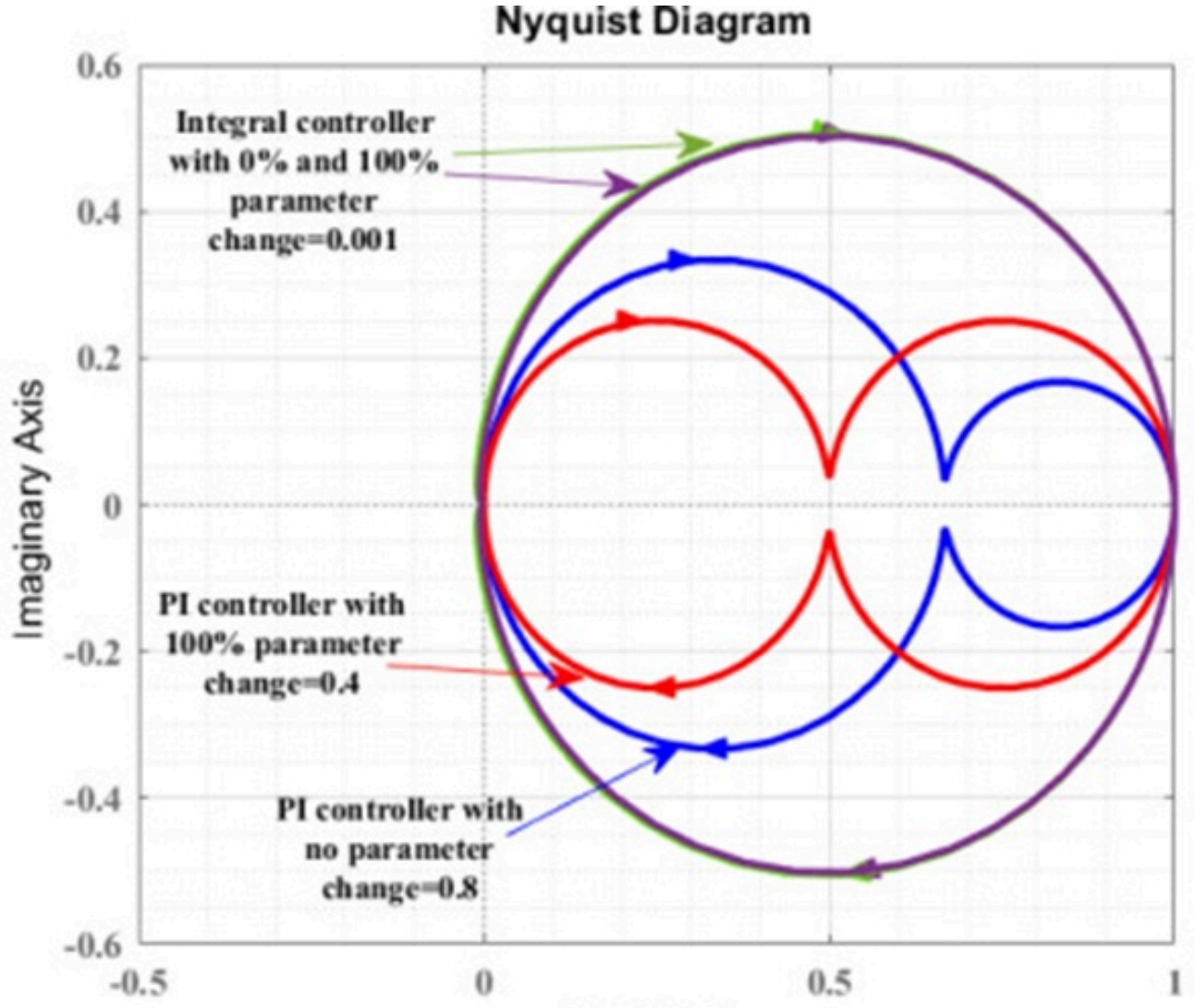
(b)

$$\frac{i_d}{i_d^*} = \frac{\cdots}{L_c' s^2 + \left(R_c' + k_{pd}\right) s + k_{id}} \quad (24)$$

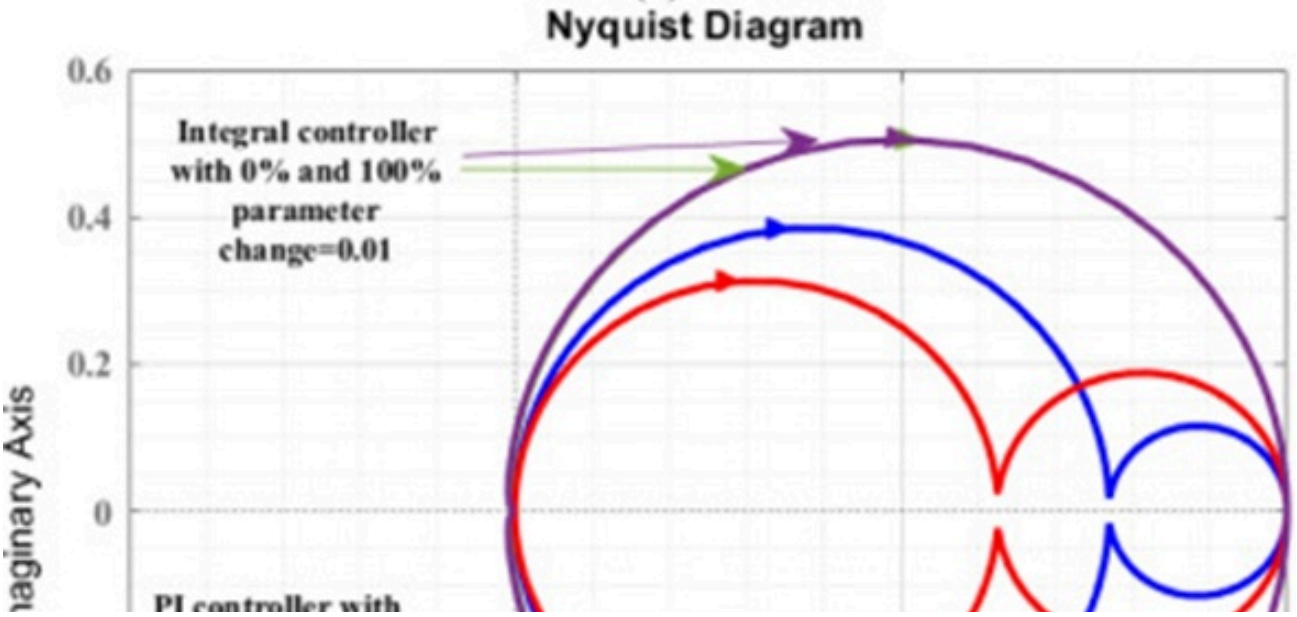
$$\left(\frac{i_q}{i_q^*}\right)^2 = \frac{k_{pq} s + k_{iq}}{0.75 p L_c' s^2 + \left(1.5 p R_c' + k_{pq}\right) s + k_{iq}} \quad (25)$$

The resulting Nyquist plots for expressions (24) and (25) are provided in **Figure 7.** The data underscore that the developed PI-driven scheme delivers excellent reference tracking performance for both components of the stator current across diverse operational conditions. As plotted, the nominal tracking gains for **Eqs. 24 and 25** stand at 0.8 and 0.91, respectively; however, these values can be adjusted closer to ideal unity by optimizing the gain parameters kpd(q) and kip(q). Moreover, **Figure 7** clearly highlights that the PI-based implementation surpasses pure integral mechanisms in both command tracking precision and dynamic resilience.

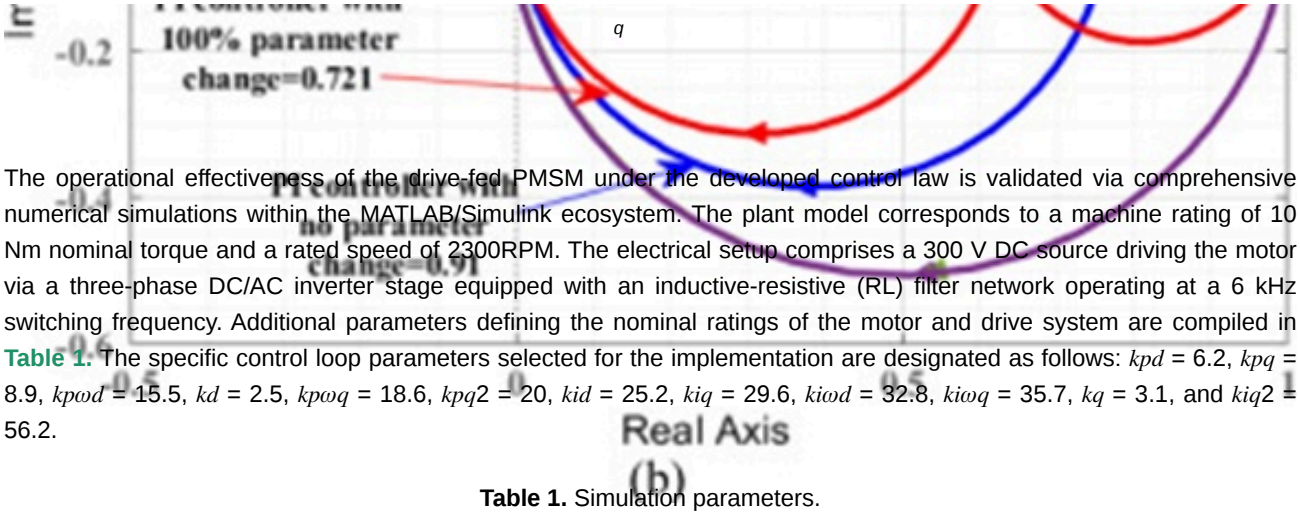
© 2024 The Author(s). | Published by Institute of Smart Energy Systems Press



(a)



© 2024 The Author(s). | Published by Institute of Smart Energy Systems Press



The operational effectiveness of the drive-fed PMSM under the developed control law is validated via comprehensive numerical simulations within the MATLAB/Simulink ecosystem. The plant model corresponds to a machine rating of 10 Nm nominal torque and a rated speed of 2300RPM. The electrical setup comprises a 300 V DC source driving the motor via a three-phase DC/AC inverter stage equipped with an inductive-resistive (RL) filter network operating at a 6 kHz switching frequency. Additional parameters defining the nominal ratings of the motor and drive system are compiled in **Table 1.** The specific control loop parameters selected for the implementation are designated as follows: kpd = 6.2, kpq = 8.9, $kp\omega d$ = 15.5, kd = 2.5, $kp\omega q$ = 18.6, $kpq2$ = 20, kid = 25.2, kiq = 29.6, $ki\omega d$ = 32.8, $ki\omega q$ = 35.7, kq = 3.1, and $kiq2$ = 56.2.

Table 1. Simulation parameters.

Parameter	Symbol	Value
Stator phase resistance	Rs	0.4578 Ω
Armature inductance	Ls	0.00134 H
Flux linkage	ϕ	0.171 Wb
Inertia	J	0.01469 kg·m²
Viscous damping	F	0.0003035 N·m·s
Number of pole pairs	p	4
Filter inductance	Lc	0.003 H
Filter resistance	Rc	0.5 Ω
Sampling time	Ts	5e−6 s

The responses of PMSM state variables under variations of load torque, DC-link voltage and system parameters

The behavior of the closed-loop system is analyzed under transient load steps, low-frequency fluctuations superimposed on the DC-bus voltage, and variations in the internal machine and inverter components. **Figure 8** charts the transient profiles of the new control framework under isolated step changes affecting the DC-bus voltage and the shaft load. Specifically, the DC-link voltage is scaled upward by a factor of 1.5 at t = 0.15 s, while the load torque is dropped to 0.7 times its rated value at t = 0.25 s. As visible in **Figure 8a,** the rotor speed is almost completely insulated from the voltage disturbance applied at t = 0.15 s. Furthermore, the speed trajectory exhibits a highly robust recovery response when the mechanical load is stepped down at t = 0.25 s.

According to **Figure 8b**, the transient settling intervals for the motor torque following these step changes are recorded at 0.001 s and 0.014 s, respectively, highlighting the controller's exceptional disturbance-rejection capabilities under aggressive dynamic shifts. The new control framework firmly regulates the d-axis component of the stator current to a zero baseline, maintaining perfect stability at both t = 0.15 s and t = 0.25 s. Conversely, the q-axis current component

© 2024 The Author(s). | Published by Institute of Smart Energy Systems Press

modulates to track the load demands, yet its transient deviations during the voltage step remain exceptionally minor, as illustrated in **Figure 8c.**

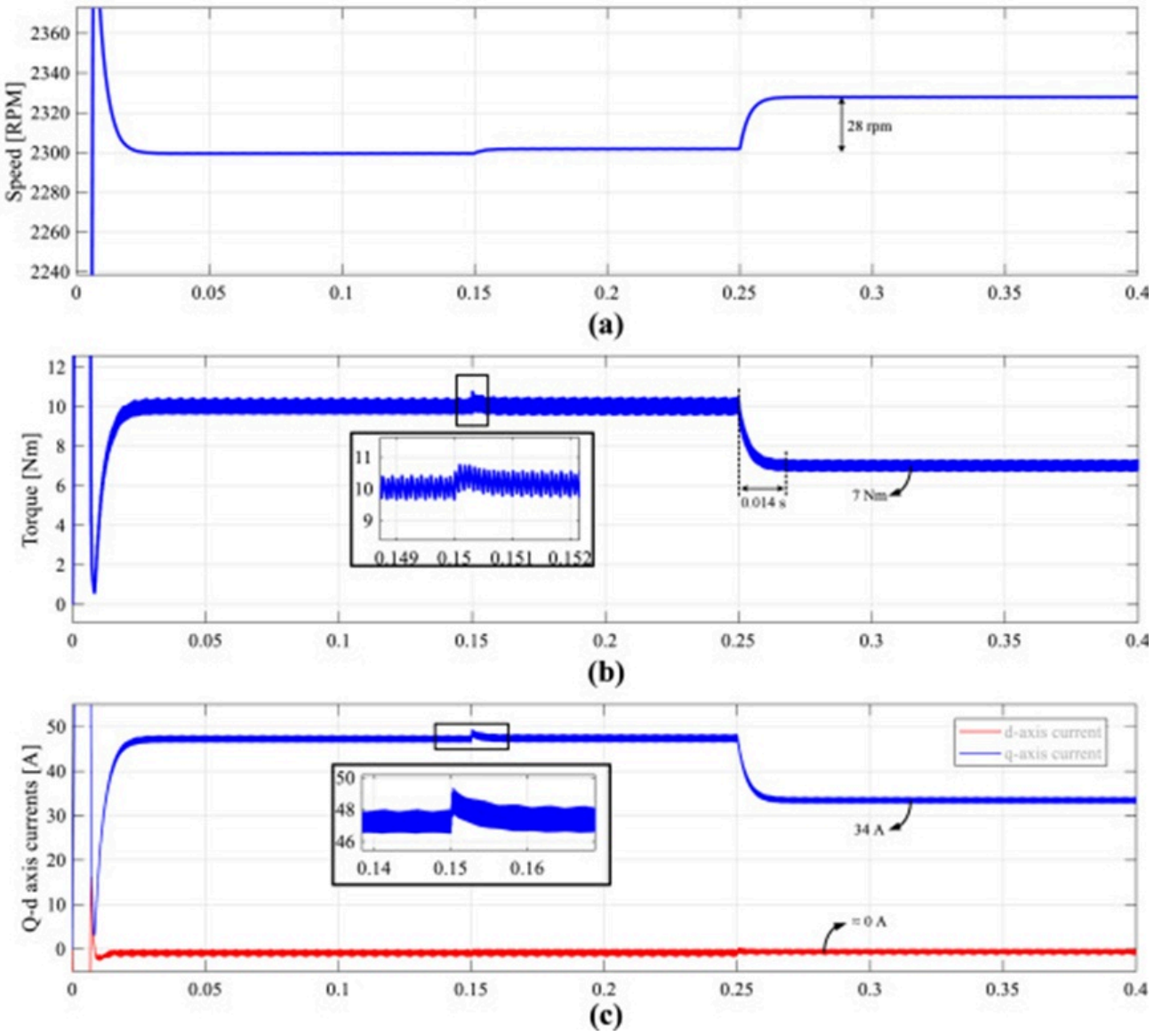


Figure 8. The steady-state and dynamic operation of the proposed control technique under the load torque and DC-link voltage variations for (a) PMSM Speed, (b) PMSM load torque, and (c) q and d components of PMSM stator current.

To evaluate parameter sensitivity across **Figures 9-13**, the machine and drive coefficients are set to bounded states defined by $\left(L_{c(s)}^{'} = 1.5L_{c(s)},\ \ R_{c(s)}^{'} = 1.5R_{c(s)}\right)$ and $\left(L_{c(s)}^{'} = 0.65L_{c(s)},\ \ R_{c(s)}^{'} = 0.65R_{c(s)}\right)$. The influence of these structural changes on motor performance is examined across two test branches. In addition to the voltage and load steps used previously, the plant parameter values are scaled up by 1.5 times and down by 0.65 times.

As captured in **Figure 9a**, during the DC-bus voltage perturbation, scaling the internal parameters upward and downward induces a maximum torque overshoot of 4% and an undershoot of only 1.2%, respectively. Furthermore, parameter fluctuations do not produce any noticeable degradation in torque regulation during the mechanical load transition at t = 0.25 s, as demonstrated in **Figure 9b.** These dynamic trends confirm the high decoupling capability and resilience of the new control framework regarding electromagnetic torque tracking.

© 2024 The Author(s). | Published by Institute of Smart Energy Systems Press

An identical test baseline involving the voltage disturbance at t = 0.15 s and the primary load step at t = 0.25 s is conducted on the drive system under nominal parameter conditions (without parameter mismatches). The corresponding steady-state and dynamic trajectories for both motor speed and torque under this baseline run are detailed in **Figure 10**. As shown in **Figures 10a and 10b**, the electromagnetic torque undergoes a brief, minor undershoot following the voltage step, while a negligible tracking offset is temporarily introduced into the rotor speed. Once the system crosses the t = 0.25 s threshold, both variables swiftly converge back to their targeted steady-state values with highly accelerated settling times.

Under the same conditions, **Figure 11** charts the steady-state and transient waveforms of the d- and q-axis stator currents subject to parametric deviations. The plots reveal that the q-axis current exhibits slightly higher steady-state offsets and dynamic deviations than its d-axis counterpart. Nonetheless, these minor variations remain functionally insignificant and do not affect output torque tracking accuracy, as confirmed by comparing **Figure 9** and **Figure 11**. This demonstrates that the designed control framework retains structural stability and high parameter insensitivity.

As dictated by the q-axis control loop architecture in **Figure 2b**, the power tracking error is integrated into the q-axis control action. **Figure 12** visualizes the steady-state and transient responses of this output power under plant parameter drift during the voltage and load steps at t = 0.15 s and t = 0.25 s, respectively. The data show that the output power tracking maintains exceptionally small steady-state discrepancies and displays highly rapid recovery characteristics, verifying its robust capability across all tested disturbances.

Finally, **Figure 13** maps the mechanical torque profile against the q-axis stator current under varying parameter conditions. The curve indicates that an upward shift in the component parameters slightly increases the q-axis current demand. Nevertheless, when measured against the nominal baseline scenario, the intrinsic robustness of the developed control strategy effectively constrains the system trajectories close to the target operational targets, as shown in **Figure 13.**

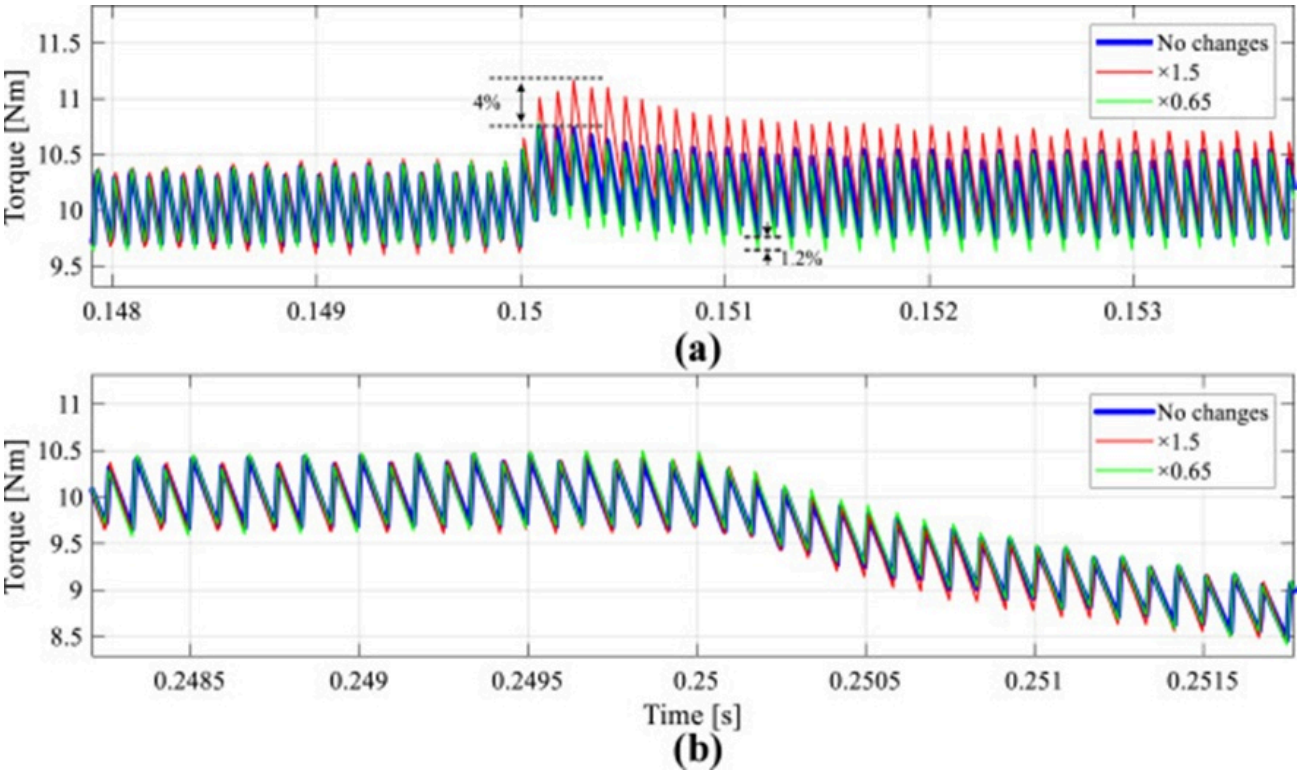


Figure 9. The steady-state and dynamic responses of the PMSM torque when changes in the PMSM parameters occur under (a) DC voltage change, and (b) load torque change.

© 2024 The Author(s). | Published by Institute of Smart Energy Systems Press

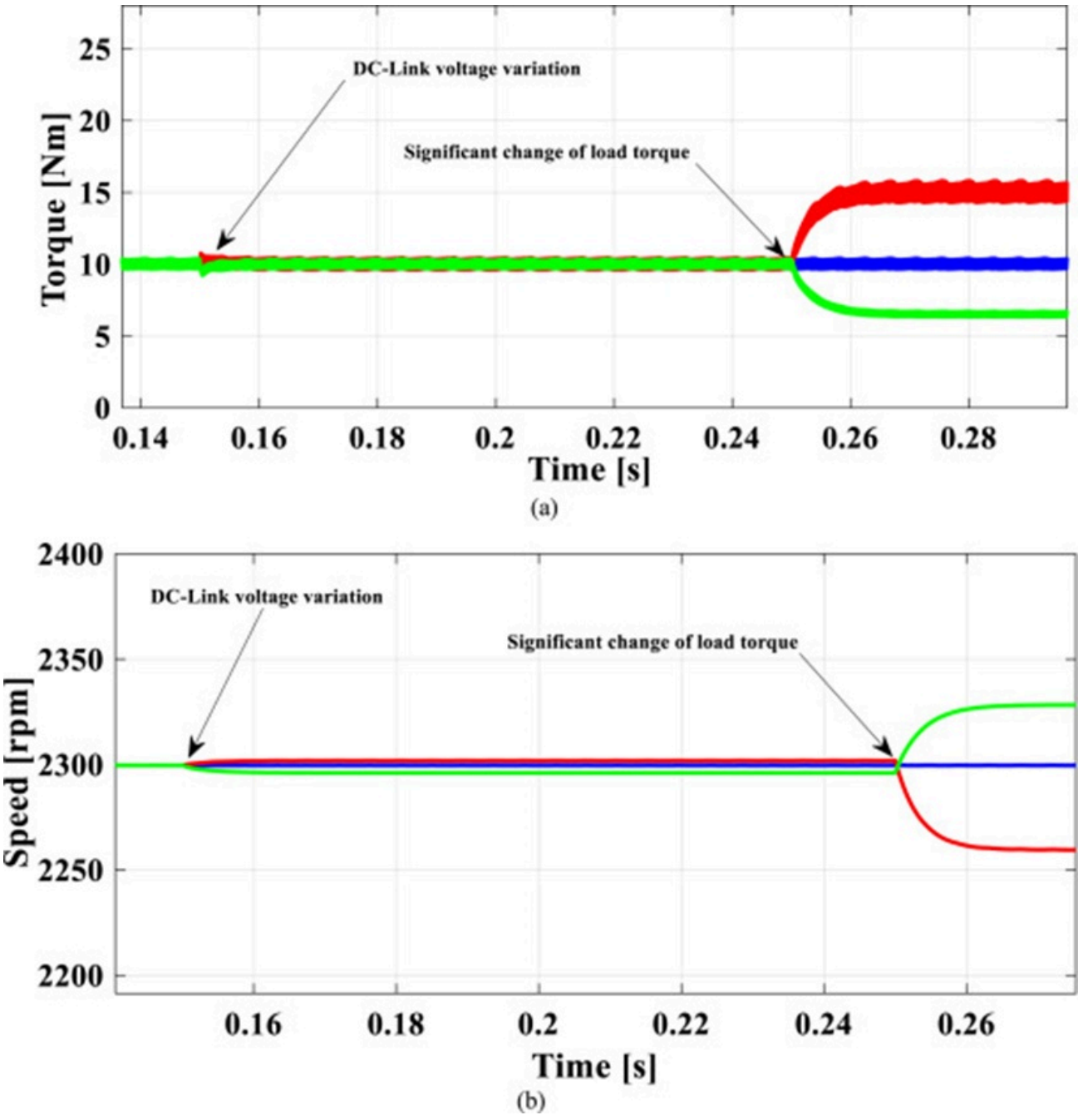


Figure 10. The steady-state and dynamic responses of the PMSM torque and speed while the DC-link voltage and load torque variations occur at t = 0.15 s and t = 0.25 s, respectively.

© 2024 The Author(s). | Published by Institute of Smart Energy Systems Press

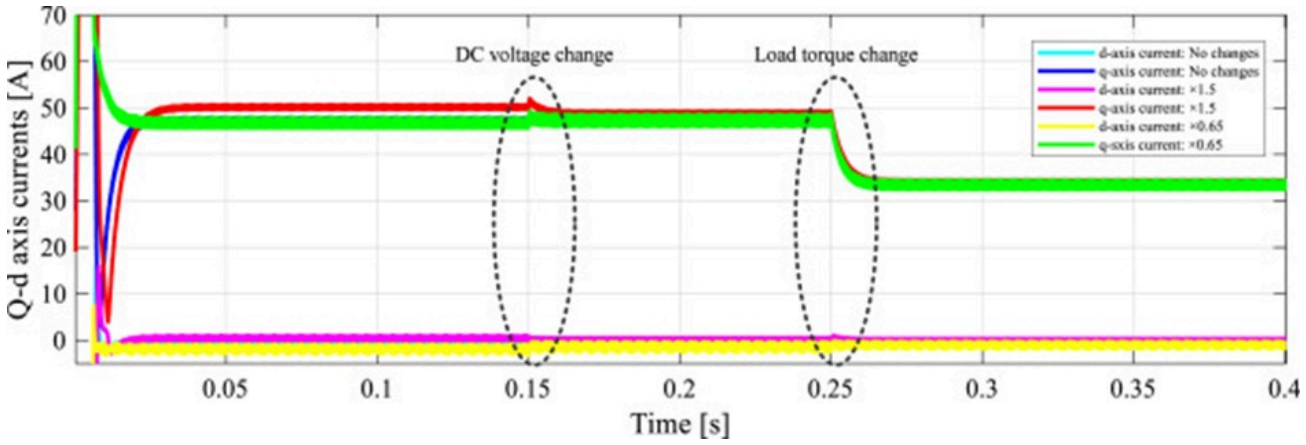


Figure 11. The steady-state and dynamic responses of the q and d components of PMSM stator current under the parameter changes while the DC-link voltage and load torque variations occur at t = 0.15 s and t = 0.25 s, respectively.

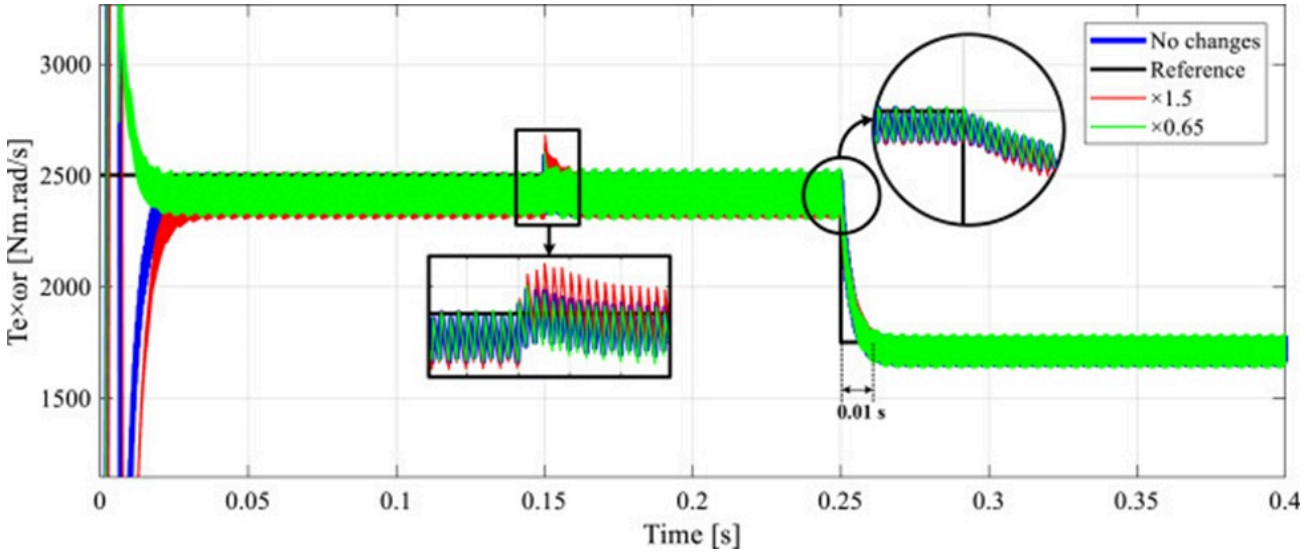


Figure 12. The steady-state and dynamic responses of the $Te \times \omega$ in the presence of parameter alterations while the DC-link voltage and load torque variations occur at t = 0.15 s and t = 0.25 s, respectively.

© 2024 The Author(s). | Published by Institute of Smart Energy Systems Press

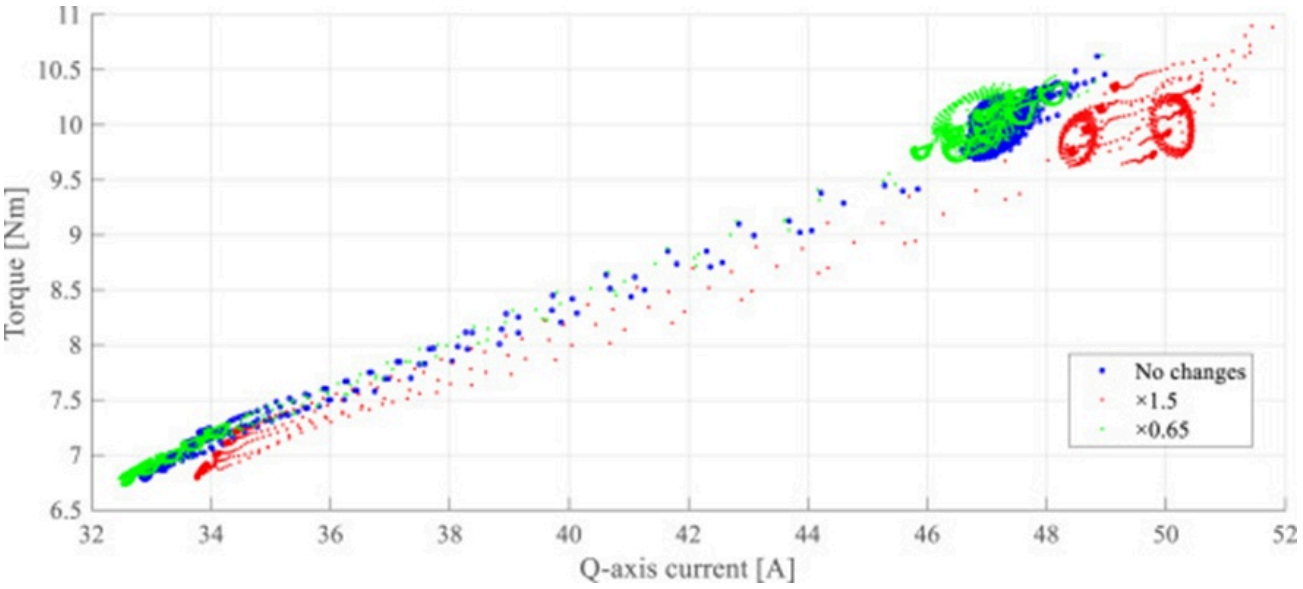


Figure 13. The PMSM torque versus the q-component of PMSM stator current.

Comparison with a conventional PI controller

In this subsection, the performance of the PMSM drive is additionally evaluated using a standard proportional-integral (PI) control system. This traditional benchmark architecture features dual control loops for velocity and current regulation operating under a zero id constraint. To facilitate a rigorous comparative assessment, two distinct operational scenarios are implemented: a mechanical load is applied to the PMSM, and a step adjustment to the speed reference is introduced at t = 0.05 s. **Figure 14** illustrates the temporal profiles of the PMSM speed and electromagnetic torque, alongside their respective transient behaviors under both the proposed control technique and the conventional PI controller during the step modification of the load. The gain parameters for the baseline PI architecture were initially established using the Ziegler–Nichols method, followed by manual empirical fine-tuning to optimize performance characteristics, aiming for a smooth transition devoid of overshoot. As observed in **Figures 14a and 14b**, the newly developed control loop forces the PMSM speed and torque to converge to their targeted references with a more rapid dynamic tracking capability than the conventional PI scheme. Nonetheless, the electromagnetic torque waveform under the proposed framework exhibits slightly more high-frequency oscillation than the standard PI configuration, though this variance remains functionally negligible.

Figure 15 depicts the steady-state and transient profiles of the PMSM speed and q-axis current under the introduced control strategy and the standard PI controller when the motor speed undergoes a step command alteration, as shown in **Figure 15a.** Based on the trajectories in **Figure 15, i**ntegrating the proposed control system into the PMSM drive yields an accelerated dynamic response and a lower steady-state tracking error than the classic PI methodology. This enhancement is due to the precise and agile reaction of the q-axis stator current against the velocity step command. Quantitative metrics derived from **Figure 15** demonstrate that, relative to the conventional PI setup, the developed control framework enables the motor speed and torque trajectories to reach 50% and 95% of their desired values while reducing the required time by 42.9% and 28.6%, respectively. Furthermore, the transient undershoot deviations in the speed and torque responses under the proposed technique are minimized by 75% compared to the standard PI design. Beyond the baseline PI controller, the efficacy of the developed strategy is evaluated against two alternative advanced methodologies from the literature: a fractional-order PID controller designed via Bode's ideal transfer function (BITF-FOPID) [35] and a particle swarm optimization-based fractional-order PID controller (PSO-FOPID) [35]. Utilizing the proposed control framework, the maximum overshoot magnitude and the associated settling interval are reduced by up to 75% and 28.6%–

© 2024 The Author(s). | Published by Institute of Smart Energy Systems Press

42.9%, respectively. In contrast, the BITF-FOPID approach diminishes the overshoot level and settling duration by up to 28.71% and 28%, respectively. In comparison, the corresponding reductions achieved via the PSO-FOPID scheme are limited to 12.2% and 9.67%, respectively.

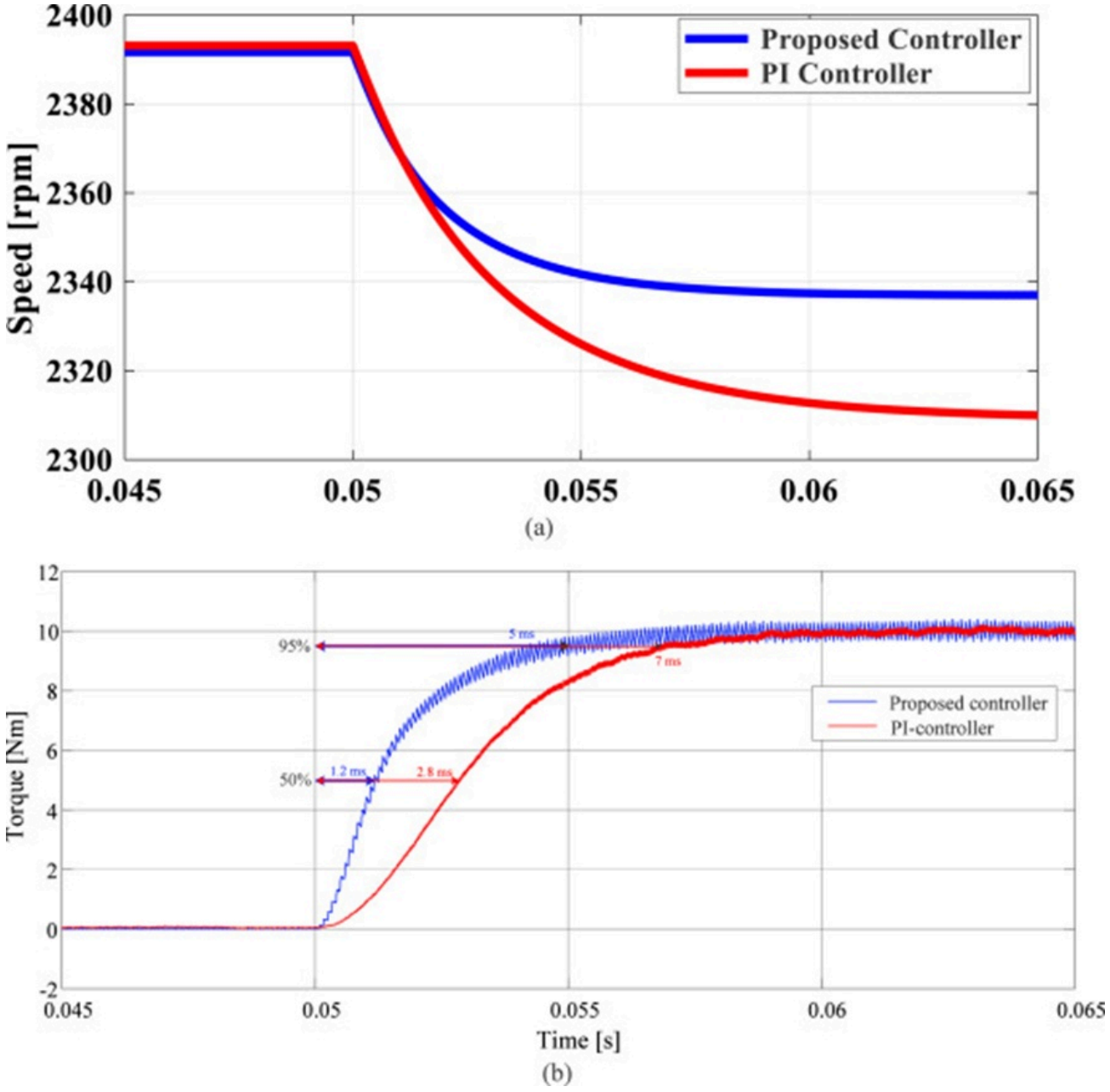


Figure 14. Comparison of transient behavior at the step change of load: (a) Speed, and (b) Torque.

© 2024 The Author(s). | Published by Institute of Smart Energy Systems Press

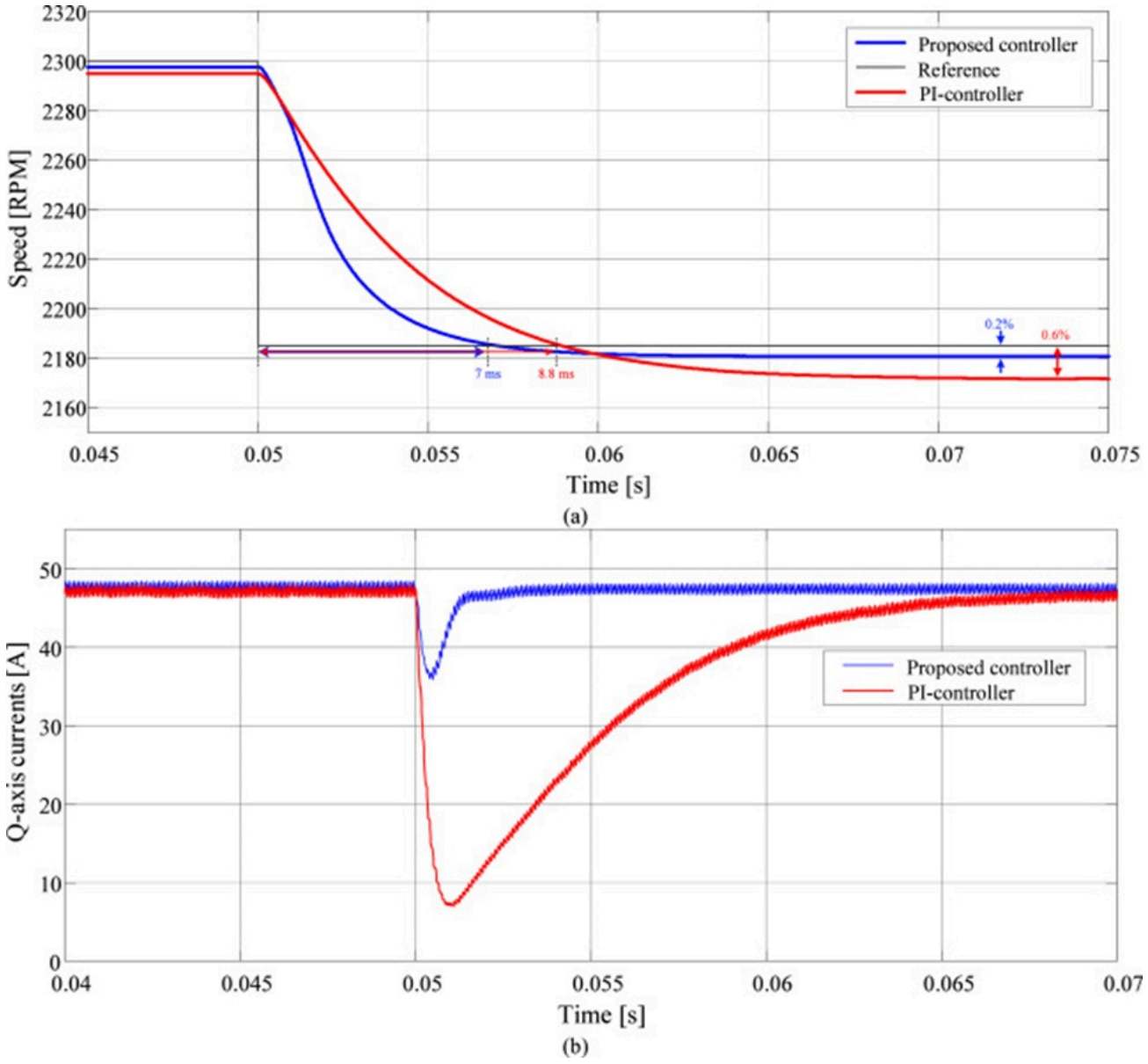


Figure 15. Comparison of transient behavior at the step change of speed: (a) speed, (b) q-axis current.

Conclusion

This study focused on the formulation of an advanced control strategy for a PMSM drive system to guarantee robust steady-state operation and highly stable dynamic behavior amidst variations in the drive's DC-link voltage and structural plant parameters. To construct this control architecture, an updated mathematical formulation was first established, enabling comprehensive compensation for tracking errors in both the d-axis component and the squared q-axis component of the stator currents. To further optimize the transient response capabilities of the introduced methodology, multiple dedicated compensating loops were engineered to suppress the adverse impacts of rotor angular frequency errors, the variance between electromagnetic and load torques, and the output power error of the drive stage. A general operating curve (GOC) was introduced to systematically analyze and bound the behavior of the PMSM stator currents. Additionally, a rigorous closed-loop stability analysis was detailed to decouple and evaluate the influence of individual controller gains precisely. Ultimately, analytical evaluations and comparative simulation runs carried out within the

© 2024 The Author(s). | Published by Institute of Smart Energy Systems Press

MATLAB/Simulink environment validated the superior performance and fidelity of the presented control strategy across a variety of demanding dynamic operational profiles.

Abbreviations

PMSM = Permanent Magnet Synchronous Motor

GOC = General Operation Curve

DC = Direct Current

AC = Alternating current

Parameters

Ls, Rs	PMSM Stator Inductance and Resistance
Lc, Rc	PMSM Drive Inductance and Resistance
,	Inaccurate parameters of PMSM Stator
,	Inaccurate parameters of PMSM Drive
ΔL_s, ΔR_s	Error of PMSM Stator Parameters
ΔL_c, ΔR_c	Error of PMSM Drive Parameters
p	Pole Pairs of PMSM
J	Moment of Inertia of PMSM
B	PMSM Friction Coefficient
C	PMSM Drive Input Capacitor
$_{(d,)}$, $k_{i\omega(d,q)}$	Compensator Coefficients of PMSM Rotor Angular Frequency Error
$_{(d,)}$, $k_{(d,q)}$	Compensator Coefficients of PMSM Drive Currents
$k_{\beta(d,q)}$	Compensator Coefficients of PMSM Electrical and Load Torque Errors

Variables

i_d, i_q	d-q Components of PMSM Drive Currents
v_{dc}	DC Link Voltage
ω_r	PMSM Rotor Angular Frequency
T_e, T_L	PMSM Electrical and Load Torque
φ	PMSM Flux

© 2024 The Author(s). | Published by Institute of Smart Energy Systems Press

i_{dc}	PMSM Drive DC Link Current
u_d, u_q	Control Input of PMSM Drive
$_d$, $_q$	Derivative of d-q Components of PMSM Drive Currents
v_d, v_q	d-q Components of PMSM Drive Voltages
$_{dc}$	Derivative of DC Link Voltage
$\Delta\omega_r$	PMSM Rotor Angular Frequency Error
ΔT_e, ΔT_L	PMSM Electrical and Load Torque Errors

Acknowledgements

None

Conflict of interest

None

Financial support

None

Ethics statement

None

Received: 17 Mar 2023 Revised: 22 May 2023 Accepted: 08 Jun 2023
Published online: 15 November 2024

Rights and permissions

Open Access The author(s) retain copyright. This article is licensed under the Creative Commons Attribution-NonCommercial-ShareAlike 4.0 International License. It may be shared and adapted for non-commercial purposes with appropriate attribution, an indication of changes, and distribution of adaptations under the same license. Third-party material may be subject to separate terms identified in its credit line. View the license at https://creativecommons.org/licenses/by-nc-sa/4.0/.

References

1. Sain C, Banerjee A, Biswas PK. Modelling and comparative dynamic analysis due to demagnetization of a torque controlled permanent magnet synchronous motor drive for energy-efficient electric vehicle. ISA Trans. 2020;97:384-400.

2. Mynar Z, Vesely L, Vaclavek P. PMSM model predictive control with field-weakening implementation. IEEE Trans Ind Electron. 2016;63(8):5156-66.

3. Lai C, Feng G, Mukherjee K, Loukanov V, Kar NC. Torque ripple modeling and minimization for interior PMSM considering magnetic saturation. IEEE Trans Power Electron. 2018;33(3):2417-29.

4. Liang W, Fei W, Luk PC-K. An improved sideband current harmonic model of interior PMSM drive by considering magnetic saturation and cross-coupling effects. IEEE Trans Ind Electron. 2016;63(7):4097-104.

5. Grobler AJ, Holm SR, Schoor GV. A two-dimensional analytic thermal model for a high-speed PMSM magnet. IEEE Trans Ind Electron. 2015;62(11):6756-64.

6. Yi P, Sun Z, Wang X. Research on PMSM harmonic coupling models based on magnetic co-energy. IET Electr Power Appl. 2019;13(4):571-9.

7. Li H, Zhang X, Yang S, Liu S. Unified graphical model of high-frequency signal injection methods for PMSM sensorless control. IEEE Trans Ind Electron. 2020;67(6):4411-21.

8. Ye S. Design and performance analysis of an iterative flux sliding-mode observer for the sensorless control of PMSM drives. ISA Trans. 2019;94:255-64.

9. Inoue T, Inoue Y, Morimoto S, Sanada M. Mathematical model for MTPA control of permanent-magnet synchronous motor in stator flux linkage synchronous frame. IEEE Trans Ind Appl. 2015;51(5):3620-8.

10. Cai R, Zheng R, Liu M, Li M. Robust control of PMSM using geometric model reduction and μ-synthesis. IEEE Trans Ind Electron. 2018;65(1):498-509.

11. Jarzebowicz L. Errors of a linear current approximation in high-speed PMSM drives. IEEE Trans Power Electron. 2017;32(11):8254-7.

12. Feng G, Lai C, Kelly M, Kar NC. Dual three-phase PMSM torque modeling and maximum torque per peak current control through optimized harmonic current injection. IEEE Trans Ind Electron. 2019;66(5):3356-67.

13. Liu H, Li S. Speed control for PMSM servo system using predictive functional control and extended state observer. IEEE Trans Ind Electron. 2012;59(2):1171-83.

14. Wang Z, Yu A, Li X, Zhang G, Xia C. A novel current predictive control based on fuzzy algorithm for PMSM. IEEE J Emerg Sel Top Power Electron. 2019;7(2):990-1001.

15. Gong C, Hu Y, Gao J, Wang Y, Yan L. An improved delay-suppressed sliding-mode observer for sensorless vector-controlled PMSM. IEEE Trans Ind Electron. 2020;67(7):5913-23.

16. Zhang X, Sun L, Zhao K, Sun L. Nonlinear speed control for PMSM system using sliding-mode control and disturbance compensation techniques. IEEE Trans Power Electron. 2013;28(3):1358-65.

17. Li S, Zhou M, Yu X. Design and implementation of terminal sliding mode control method for PMSM speed regulation system. IEEE Trans Ind Informat. 2013;9(4):1879-91.

18. Wang G, Zhang H. A new speed adaptive estimation method based on an improved flux sliding-mode observer for the sensorless control of PMSM drives. ISA Trans. 2022;128(Pt A):675-85.

19. Yang T, Deng Y, Li H, Sun Z, Cao H, Wei Z, et al. Fast integral terminal sliding mode control with a novel disturbance observer based on iterative learning for speed control of PMSM. ISA Trans. 2022. https://doi.org/10.1016/j.isatra.2022.10.011.

© 2024 The Author(s). | Published by Institute of Smart Energy Systems Press

20. Liu J, Li H, Deng Y. Torque ripple minimization of PMSM based on robust ILC via adaptive sliding mode control. IEEE Trans Power Electron. 2018;33(4):3655-71.

21. Gabbi TS, de Araujo MB, Rocha LR, Scalcon FP, Gründling HA, Vieira RP. Discrete-time sliding mode controller based on backstepping disturbance compensation for robust current control of PMSM drives. ISA Trans. 2022;128(Pt A):581-92.

22. Ganapathee M, Alavandar S, Kasinathan P, Sowmmiya U, Ramachandaramurthy VK, Pachaivannan N. Evaluation of hybrid controllers for space vector modulation-inverter driven permanent magnet synchronous motor-pump assembly. ISA Trans. 2022;128(Pt A):635-49.

23. Xu C, Han Z, Lu S. Deadbeat predictive current control for permanent magnet synchronous machines with closed-form error compensation. IEEE Trans Power Electron. 2020;35(5):5018-30.

24. Lai C, Feng G, Mukherjee K, Kar NC. Investigations of the influence of PMSM parameter variations in optimal stator current design for torque ripple minimization. IEEE Trans Energy Convers. 2017;32(3):1052-62.

25. Choi HH, Vu NTT, Jung J-W. Digital implementation of an adaptive speed regulator for a PMSM. IEEE Trans Power Electron. 2011;26(1):3-8.

26. Chou M-C, Liaw C-M. PMSM-driven satellite reaction wheel system with adjustable DC-link voltage. IEEE Trans Aerosp Electron Syst. 2014;50(2):1359-73.

27. Lee J-H, Won C-Y, Lee B-K, Kim H-B, Baek J-H, Han K-B, et al. IPMSM torque control method considering DC-link voltage variation and friction torque for EV/HEV applications. In: IEEE Veh Power Propulsion Conf (VPPC). 2012. p. 1063-9.

28. Mohamed YARI, Ahmed A, Radwan A, Lee TK. Decoupled reference-voltage-based active DC-link stabilization for PMSM drives with tight-speed regulation. IEEE Trans Ind Electron. 2012;59(12):4523-36.

29. Zhang X, Yang J. A DC-link voltage fast control strategy for high-speed PMSM/G in flywheel energy storage system. IEEE Trans Ind Appl. 2018;54(2):1671-9.

30. Yuan Q, Zhao R. DC-link capacitor voltage offset suppression with no filters for three-phase four-switch inverter fed PMSM drives. Electron Lett. 2017;53(11):746-8.

31. Shuai D, Qianfan Z, Weipan Z, Chaowei Z, Tuopu N. A compound control strategy for improving the dynamic characteristics of the DC-link voltage for the PMSM drive system based on the quasi-z-source inverter. IEEE Access. 2019;7:151929-38.

32. Ke Z, Zhang J, Degner MW. DC bus capacitor discharge of permanent-magnet synchronous machine drive systems for hybrid electric vehicles. IEEE Trans Ind Appl. 2017;53(2):1399-405.

33. Nguyen TH, Nguyen TT, Minh Le K, Tran HN, Jeon JW. An adaptive backstepping sliding-mode control for improving position tracking of a permanent-magnet synchronous motor with a nonlinear disturbance observer. IEEE Access. 2023;11:19173-85.

34. Fan Y, Chen J, Zhang Q, Cheng M. An improved inertia disturbance suppression method for PMSM based on disturbance observer and two-degree-of-freedom PI controller. IEEE Trans Power Electron. 2023;38(3):3590-9.

35. Chen P, Luo Y. Analytical fractional-order PID controller design with bode's ideal cutoff filter for PMSM speed servo system. IEEE Trans Ind Electron. 2023;70(2):1783-93.

36. Yin Y, Zhang H, Wang L, Chen X, Liu J, Zhao Q, et al. Disturbance and uncertainty attenuation for speed regulation of PMSM servo system using adaptive optimal control strategy. IEEE Trans Transp Electrif. 2023;9(2):3410-20.

37. Liu H, Lin W, Liu Z, Buccella C, Cecati C. Model predictive current control with model-aid extended state observer compensation for PMSM drive. IEEE Trans Power Electron. 2023;38(3):3152-62.

© 2024 The Author(s). | Published by Institute of Smart Energy Systems Press

38. Gaeid Khalaf S, Al Smadi Takialddin, Abubakar Ukashatu. Double control strategy of PMSM rotor speed-based traction drive using resolver. Res Control Optim. 2023;13:100301.

39. Vanchinathan K, Selvaganesan N. Adaptive fractional order PID controller tuning for brushless DC motor using artificial bee colony algorithm. Res Control Optim. 2021;4:100032.

40. Vanchinathan K, Valluvan KR, Gnanavel C, Gokul C. Numerical simulation and experimental verification of fractional-order PI controller for solar PV fed sensorless brushless DC motor using whale optimization algorithm. Electr Power Compon Syst. 2022;50(1-2):64-80.

41. Rigatos G, Siano P, AL-Numay M, Abbaszadeh M, Sari B. Nonlinear optimal and multi-loop flatness-based control of induction motor-driven desalination units. Res Control Optim. 2024;14:100360.

42. Wu T, Li M, Wang Y, Zhang L, Chen H, Zhao S, et al. Enhanced model predictive control for PMSM based on reference voltage predictive model. IEEE J Emerg Sel Top Power Electron. 2023;11(5):5290-300.

43. Holari YT, Taher SA, Mehrasa M. Power management using robust control strategy in hybrid microgrid for both grid-connected and islanding modes. J Energy Storage. 2021;39:102600.

© 2024 The Author(s). | Published by Institute of Smart Energy Systems Press